21

Ionospheric Disturbances Related to Earthquakes

Kosuke Heki

ABSTRACT

Large earthquakes disturb the ionosphere in several different ways, and we can observe them with GNSS networks as changes in TEC. First, I discuss coseismic disturbances that appear ~10 minutes after earthquakes as sudden TEC oscillations propagating toward magnetic equator with the acoustic wave speed (~1 km/s). Coseismic uplift/subsidence excite acoustic waves, and components with periods of 4–5 minutes propagate to the ionospheric F region and cause TEC oscillations. An empirical law is proposed to relate their amplitudes to moment magnitudes (M_w) of earthquakes using ~30 events M_w6.6–9.2. A very large earthquake is often followed by resonant atmospheric oscillation lasting for hours. Rayleigh surface waves also make acoustic waves and cause TEC oscillations thousands of kilometers away from epicenters. Secondly, I review current knowledge of TEC changes occurring immediately before large earthquakes. They start 10–80 minutes before earthquakes and make positive electron density anomalies above faults about to rupture. Comparison of 18 earthquakes M_w7.3–9.2 suggests positive correlations with M_w in their leading times, changes in TEC rates, and cumulative anomalies. The three-dimensional structure of electron density anomalies suggest they are formed by $\mathbf{E} \times \mathbf{B}$ drift caused by the penetration of electric fields, possibly made by surface charges, through the ionosphere.

21.1. INTRODUCTION

Fault dislocation of an earthquake causes vertical movement of the Earth's surface and excites atmospheric waves. They propagate upward and often disturb the ionosphere. Its first phase starts ~10 minutes after an earthquake, when acoustic waves reach the ionospheric F region. Such coseismic ionospheric disturbances usually occur as transient disturbances having periods of several minutes, but may last for hours after very large earthquakes. On the other hand, physical mechanisms responsible for ionospheric changes immediately before large earthquakes remain elusive. They appear as positive electron density anomalies above faults about to rupture, probably due to certain electromagnetic processes. They start 10–80 minutes before large earthquakes and build up until the fault rupture starts.

Cases of detection of earthquake-related signals have been increasing owing to the densification of receiving stations of a Global Navigation Satellite System (GNSS), such as the Global Positioning System (GPS). Because their primary purpose is crustal deformation monitoring, they are densely deployed near plate boundaries. Microwave signals from GNSS satellites are also useful in measuring ionospheric total electron content (TEC) and number of electrons integrated along the line-of-sight (LOS) connecting the receiver and the satellite. GNSS has established its status as a useful sensor to study ionospheric disturbances related to earthquakes.

Department of Earth Planetary Sciences, Hokkaido University, Sapporo-city, Japan

Coseismic ionospheric disturbances were found first by Doppler sounding as the vertical oscillation of the ionosphere (Yuen et al., 1969; Tanaka et al., 1984), and was caught first with GPS in the 1994 Northridge earthquake, California (M_w6.7) (Calais & Minster, 1995). A comprehensive study with a dense GNSS array for the 2003 Tokachi-oki earthquake, Japan (M_w8.0) (Heki & Ping, 2005), revealed various properties of the near-field disturbances, e.g. propagating velocities and directivities. Heki et al. (2006) used the TEC change waveforms in the 2004 Sumatra-Andaman earthquake (M_w9.2) to infer how rupture propagated along the long faults from northern Sumatra to the Andaman Islands. Such an acoustic disturbance may also bring about long-lasting electron depletion above the tsunami source region (Saito et al., 2011; Kakinami et al., 2012) caused by displacements of neutral atmosphere and electrons in different directions (Shinagawa et al., 2013).

Propagation of the Rayleigh surface wave also excites acoustic waves making ionospheric disturbances observed in far-fields. Ducic et al. (2003) detected ionospheric disturbances, caused by the 2002 Denali earthquake, Alaska, propagating southward with the Rayleigh wave speed in California. Large earthquakes and tsunamis also excite internal gravity waves with longer periods and make concentric wave fronts as observed after the 2011 Tohoku-oki earthquakes (Tsugawa et al., 2011). A review of atmospheric wave excitation by earthquakes is available in Tanimoto et al. (2015), and Section 21.3 of this chapter presents several new examples.

There are three independent streams in the studies of ionospheric changes prior to large earthquakes. One approach focuses on the propagation anomaly of very low frequency (VLF) radio waves. Hayakawa et al. (1996) found that the phase of VLF wave, transmitted from Kyushu and received in Kanto, started to show characteristic variation 3 days before the 1995 Kobe earthquake (M_w7.0), Japan. They considered that a certain anomaly occurred in the lower ionosphere above Kobe, just at the middle of the VLF propagation path. The launch of the DEMETER (Detection of Electro-Magnetic Emissions Transmitted from Earthquake Regions) satellite from France is related to this stream, and Němec et al. (2008) and Li & Parrot (2013) reported statistically significant anomalies in lower ionospheric electron density shortly before earthquakes.

Another stream originates from Liu et al. (2001), who found anomalous diurnal variation of ionospheric TEC from GNSS observations above the epicentral region of the 1999 Chi-chi earthquake (M_w7.7), Taiwan. They showed that the diurnal variation amplitude decreased three to four days before the earthquake. Based on the analyses of many past earthquakes, Le et al. (2011) and Thomas et al. (2017) gave positive and negative conclusions, respectively, on the statistical significance of such precursory changes.

In this chapter, I review studies in the new stream, ionospheric anomalies with much shorter timescales, say 10-80 minutes before large earthquakes. This was found after the 2011 M_w9.0 Tohoku-oki earthquake (Heki, 2011), and similar TEC changes were found immediately before most of the M_w≥8.2 earthquakes in this century. In Section 21.4 of this chapter, I give a brief history of debate, review recent works, and explain models proposed to explain their mechanisms.

21.2. GNSS-TEC OBSERVATIONS

21.2.1. Phase Difference and TEC

Satellites of GPS, the oldest GNSS, transmit microwave signals in two frequencies, ~1.5 GHz (L1) and ~1.2 GHz (L2), from altitude of ~20,200 km. The signals undergo dispersive (frequency-dependent) delays in the ionosphere. By tracking the differences between the L1 and L2 phases Δ(L1-L2), we can monitor the temporal changes of TEC along LOS (slant TEC or STEC). Their changes are related to the phase difference changes as follows (in TEC unit, i.e. 10^{16} el/m^2):

$$\Delta\text{STEC} = (1/40.308)\ f_1{}^2 f_2{}^2/\left(f_1{}^2 - f_2{}^2\right)\Delta(\text{L1} - \text{L2}).$$
$$(21.1)$$

There, $f1$ and $f2$ show the frequencies of the two microwave carriers from GNSS, and the phase difference Δ(L1-L2) should be expressed with the unit of meter. STEC shows U-shaped temporal changes coming from the apparent movement of the satellites in the sky (and consequent changes of the penetration angles of LOS to the ionosphere) and have biases. Typical sampling interval at ground GNSS stations is 30 seconds. Strong coseismic ionospheric disturbances can be well recognized in STEC time series.

There are increasing number of ground stations with receivers capable of receiving GNSS other than GPS, e.g. Russian GLONASS, European Galileo, Japanese QZSS, and Chinese Beidou. They transmit microwave signals in slightly different frequencies, which should be considered in converting the phase differences into TEC. GNSS raw data files are available as RINEX (Receiver independent exchange format) files and can be downloaded from data centers operated by, e.g. International GNSS Service (IGS), and University NAVSTAR Consortium (UNAVCO).

21.2.2. From STEC to VTEC

STEC time series include apparent U-shaped long-term (hours) changes coming from the motion of satellites, in addition to real spatial (e.g. latitudinal difference of ionization) and temporal (e.g. diurnal change) variations. For the sake of intuitive understanding of ionospheric disturbances, we often convert STEC into vertical TEC (VTEC). Conversion from STEC (usually with biases) to VTEC can be done following several steps. We first remove phase ambiguities by aligning STEC derived from carrier phases (Equation 21.1) with those derived by pseudo-ranges, which have larger noises but no phase ambiguities. Then we correct for satellite and receiver inter-frequency biases (IFBs) available online from the header information of Global Ionospheric Map (GIM) files (Mannucci et al., 1998). If the receiver bias of a station of interest is not available in GIM, we need to determine the receiver IFB by minimizing the scatter of nighttime VTEC at that station, an approach known as "minimum scalloping" (Rideout & Coster, 2006).

The coordinates of the ionospheric piercing points (IPP) of LOS are calculated assuming a thin ionosphere normally at altitude of 300 km, and the trajectories of their ground projections (sub-ionospheric points, SIP) are plotted on the map to indicate the horizontal position of the observed ionosphere. At the same time, we can calculate the incidence angle of the LOS and the hypothetical thin ionosphere. By multiplying the cosine of this angle, the bias-free STEC can be converted into absolute VTEC.

21.2.3. Isolation of Earthquake-Origin Signals

Ionospheric disturbances by earthquakes are over-printed to VTEC changes, which include regular diurnal changes, spatial changes due to movement of IPP (i.e. crossing of equatorial ionization anomalies), short-term (a few minutes) positive pulses caused by sporadic-E (Es) irregularities (e.g. Maeda and Heki, 2015), sudden drops due to plasma bubbles, large-scale traveling ionospheric disturbances (LSTID) (e.g. Saito et al., 1998), medium-scale traveling ionospheric disturbances (MSTID) (e.g. Otsuka et al., 2011), and so on.

Coseismic ionospheric disturbances have longer periods than typical Es signatures but have shorter periods than traveling disturbances such as MSTID and LSTID. They can be isolated by applying a high-pass filter, typically done by modeling the VTEC (or STEC) changes with polynomials of time (appropriate degree depends on the time window) and by extracting the departures from these reference curves. Such disturbances usually appear as N-shaped TEC disturbances 10–15 minutes after the main shock (see Section 21.3 for detail) with amplitudes of a few TECU. Because they propagate outward from the epicenter with several prescribed velocities, it is usually easy to distinguish them from other disturbances. In distance-time diagrams shown in Section 21.3, I used a wavelet to isolate components with period of 4–5 minutes as described in Heki & Ping (2005).

Because preseismic ionospheric changes have longer timescales (10–80 minutes), isolation of their signals is less straightforward depending on the ionospheric conditions. It often works well to subtract the best-fit polynomials whose coefficients are estimated excluding a certain period affected by the disturbances. However, objective determination of the start and end of the disturbance is often difficult, and it needs a special care to isolate preseismic anomalies. These issues are discussed in detail in He & Heki (2017).

21.3. COSEISMIC IONOSPHERIC DISTURBANCES

21.3.1. General Description

Figure 21.1 illustrates mechanisms of three types of atmospheric waves that are excited by earthquakes, propagate upward, and may disturb the ionosphere. First, direct acoustic wave, excited by coseismic vertical crustal movement above the ruptured fault, propagates upward just like the P-wave propagates in the solid earth. It reaches the F region of ionosphere in ~10 minutes and leaves N-shaped oscillation in TEC. Due to large geometric decay, this type of disturbance can be seen in near-fields, typically within one thousand kilometers. Part of the acoustic wave comes back to the ground by atmospheric refraction and is detected by infrasound sensors (Le Pichon et al., 2005).

Internal gravity wave is also excited and propagates obliquely upward from the focal area and/or propagating tsunami. It has longer periods, and propagates more slowly than the acoustic waves (e.g. Occhipinti et al., 2006). Secondary acoustic waves are excited when the Rayleigh wave propagates the Earth's surface (e.g. Rolland et al., 2011a). Due to smaller geometric decay, they often disturb the ionosphere thousands of kilometers away from epicenters. Vertical movements of charged particles in the geomagnetic field induce electric currents in ionosphere and cause geomagnetic pulsation (Iyemori et al., 2005).

21.3.2. Near-Field Disturbance

Near-field coseismic ionospheric disturbances are the ionospheric response to upward propagating acoustic waves excited at the surface by coseismic crustal uplift/subsidence above the epicenter. In Figure 21.2, I show the TEC disturbances appearing ~10 minutes after the
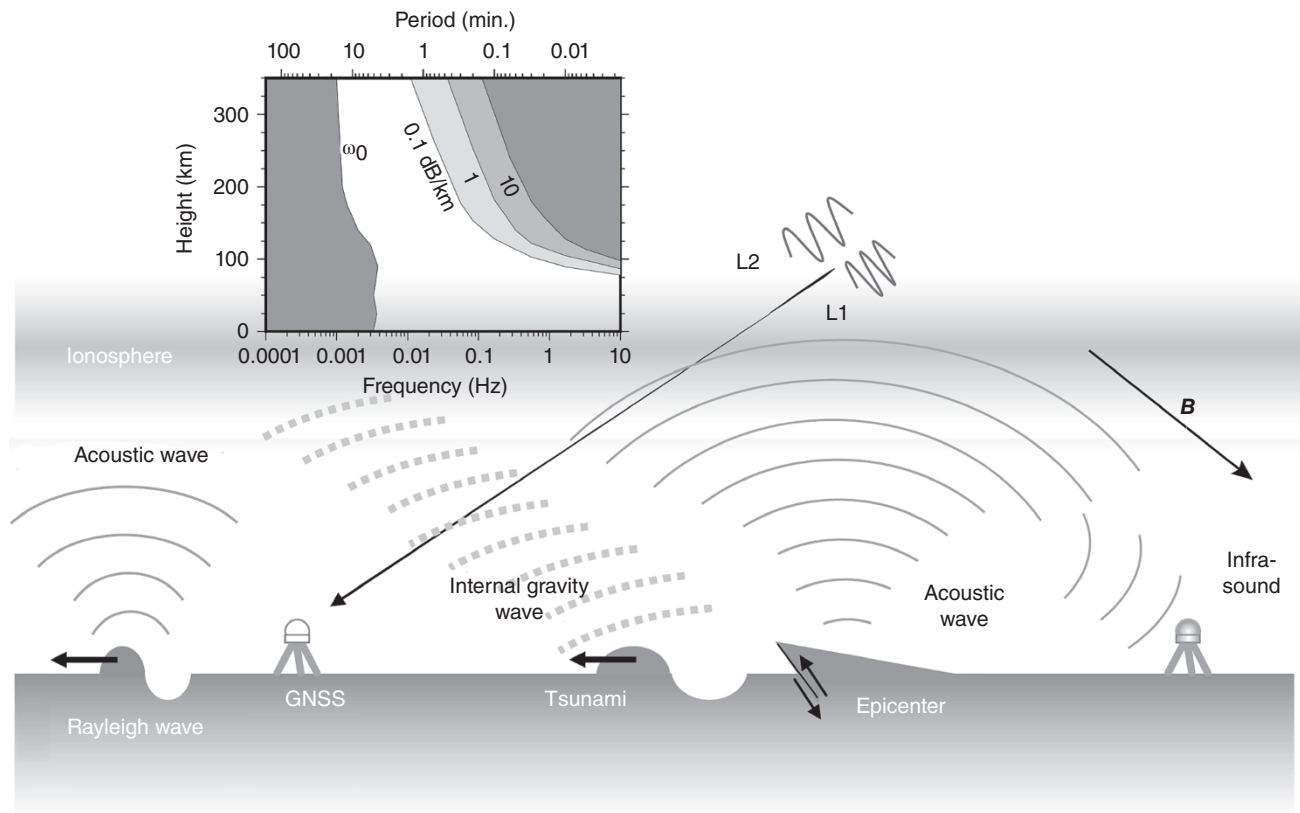
Figure 21.1 Three kinds of atmospheric waves excited by earthquakes disturb ionosphere and can be observed with GNSS as TEC changes, i.e. (1) direct acoustic wave from the focal area; (2) gravity wave propagating obliquely upward from the focal area and/or propagating tsunami; and (3) secondary acoustic wave excited by the Rayleigh surface wave. Part of the direct acoustic wave comes back to the ground by atmospheric refraction as infrasound. Modified from Figure 2 in Heki et al. (2006). Inset shows the frequency dependent atmospheric filtering effect of acoustic waves after Blanc (1983).

1994 M_w8.3 Hokkaido-Toho-Oki earthquake observed by GEONET, the Japanese dense network of GNSS receivers (Astafyeva et al., 2009). Figure 21.2a,d shows STEC anomalies as functions of time (horizontal axis) and distance (vertical axis). Positive anomalies (red) indicate the passage of coseismic ionospheric disturbances, and the slope of the line connecting the red parts corresponds to the propagation speed of the anomalies. A notable feature is that the anomalies show two different propagating velocities of ~0.8 km/s and ~4 km/s. They are ionospheric disturbances caused by direct acoustic waves and by Rayleigh surface waves, respectively.

The individual waveforms (Figure 21.2b,e) are characterized by N-shaped waves starting with narrow positive pulses followed by subsequent broad negative changes. At the source of this earthquake, crustal uplift occurs as a step function. It makes a wave with compression at their front and rarefaction behind them, and they make the positive and negative electron density anomalies in ionosphere. The wave propagates upward, gradually changing its direction due to refraction, and a part of it propagates almost horizontally at ionospheric altitudes

(see Figure 7 of Heki & Ping, 2005). When LOSs penetrate the regions with positive and negative ionospheric electron density anomalies, TEC shows positive and negative changes.

Due to the atmospheric filtering effect (Blanc, 1985) (Figure 21.1 inset), only frequency components with periods of a few minutes can travel to ionosphere without severe attenuation. In the case of coseismic ionospheric disturbance, the original atmospheric waves would have a wide range of frequency spectra, but those close to the acoustic cut-off (periods 4–5 minutes) would survive at the ionospheric height as seen in Figure 21.2b,e.

21.3.3. Atmospheric Resonance

Atmospheric acoustic waves generated at the surface propagate vertically. The waves reflect downward at mesopause and interfere with the upward propagating waves, and cause resonant oscillation (Tahira, 1995; Shinagawa et al., 2007). Acoustic resonance in 3.7 mHz and 4.4 mHz is found in the Earth's background free oscillation (Nishida et al., 2000), and these frequencies were
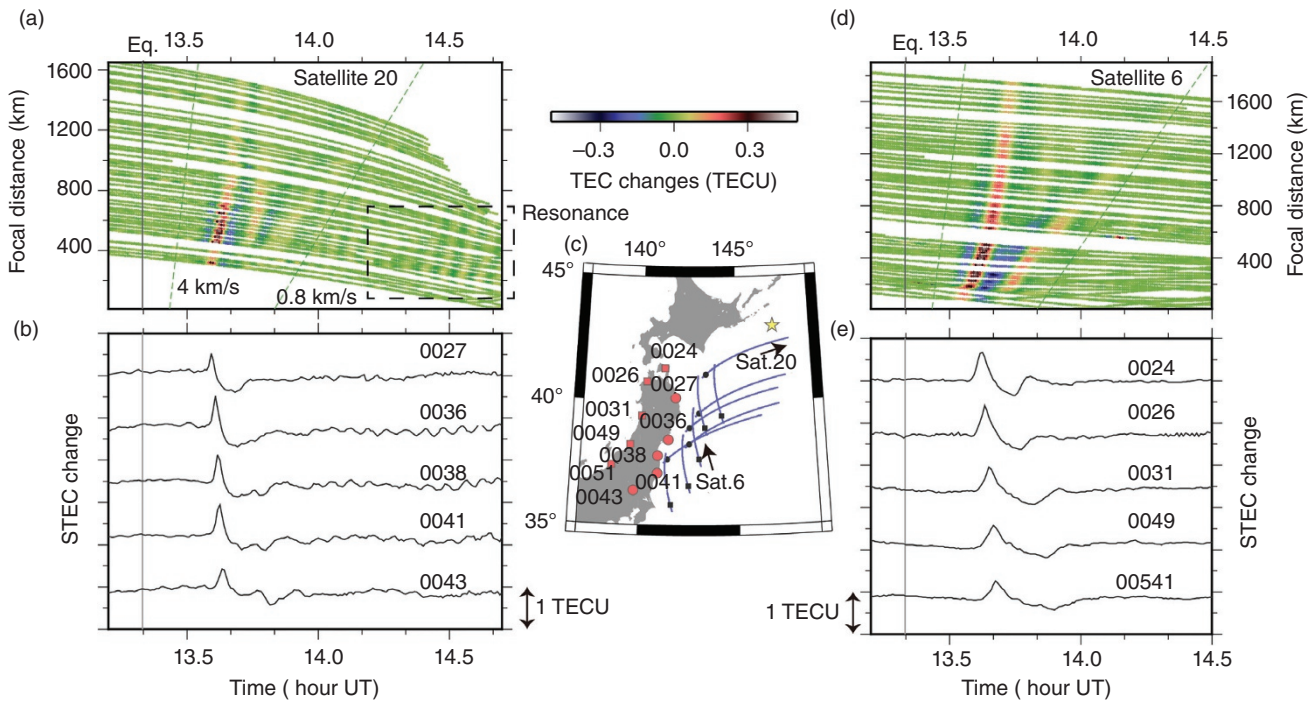
Figure 21.2 Time series of TEC response to the 1994 Oct. 04 Hokkaido-Toho-Oki earthquake (M_w8.3) observed with the GPS satellites 20 (b) and 6 (e) at ground stations shown in (c) as red squares and circles, respectively. The vertical gray lines on the panels indicate the time of the main shock. Distance-time diagram of the ionospheric disturbances, isolated by using a wavelet (Heki & Ping, 2005), are given for GPS satellite 20 (a) and 6 (d). One curve corresponds to a pair of a station and a satellite and the colors show TEC anomalies. Thin curves in (c) show trajectories of SIP, and the circles/squares on them correspond to SIP positions at the mainshock. The yellow star represents the epicenter. Atmospheric resonant oscillation signatures are seen ~1 hour after earthquakes with satellite 6 (a).

identified in postseismic TEC oscillation by GNSS-TEC after the 2004 Sumatra-Andaman earthquake (Choosakul et al., 2009), the 2011 Tohoku-oki earthquake (Saito et al., 2011; Rolland et al., 2011b), the 2007 Bengkulu earthquake (Cahyadi & Heki, 2013), and the 2012 North Sumatra earthquakes (Cahyadi & Heki, 2015). They are evanescent waves in the ionosphere caused by modes in the lower part of the atmosphere.

The examples in Figure 21.2a,b show clear oscillation in this frequency. With a closer look, this oscillation is found to propagate away from the epicenter with the Rayleigh surface wave speed (~4 km/sec). This suggests that the Airy phase of the surface wave efficiently coupled with the atmosphere and increased the amplitudes of the forced oscillation of the atmosphere by resonance. Such atmospheric harmonic oscillations also occur during strong Plinian eruptions of volcanoes (Nakashima et al., 2016; Shults et al., 2016).

21.3.4. Directivity

Heki & Ping (2005) reported the N–S asymmetry of coseismic ionospheric disturbance of the 2003 Tokachi-oki earthquake, Japan, i.e. they propagated little northward, and attributed it to the interaction with the geomagnetic field. If particle motions of neutral atmosphere in the F region are perpendicular to the magnetic field, electrons do not move together with neutral particles and the electron density anomalies do not emerge. In the mid-latitude region of the northern hemisphere, this happens to the north of the epicenter. Such a N–S asymmetry is also seen in the ionospheric responses to Vulcanian explosions of volcanoes (Heki, 2006). Rolland et al. (2013) mapped the coseismic ionospheric disturbance amplitudes at stations with various azimuths around the epicenter of the 2011 Van earthquake, Turkey, and succeeded in reproducing such N–S asymmetry with realistic numerical simulations.

This directivity will reverse in the southern hemisphere, i.e. the coseismic ionospheric disturbances propagate only northward. Such directivity was first confirmed for the 2004 Sumatra-Andaman earthquake (M_w9.2) by Otsuka et al. (2006), and later by Cahyadi & Heki (2015) for the 2012 April North Sumatra earthquake (M_w8.6) and its largest aftershock (M_w8.2). These earthquakes occurred in the northern hemisphere but are located to the south of the magnetic equator.
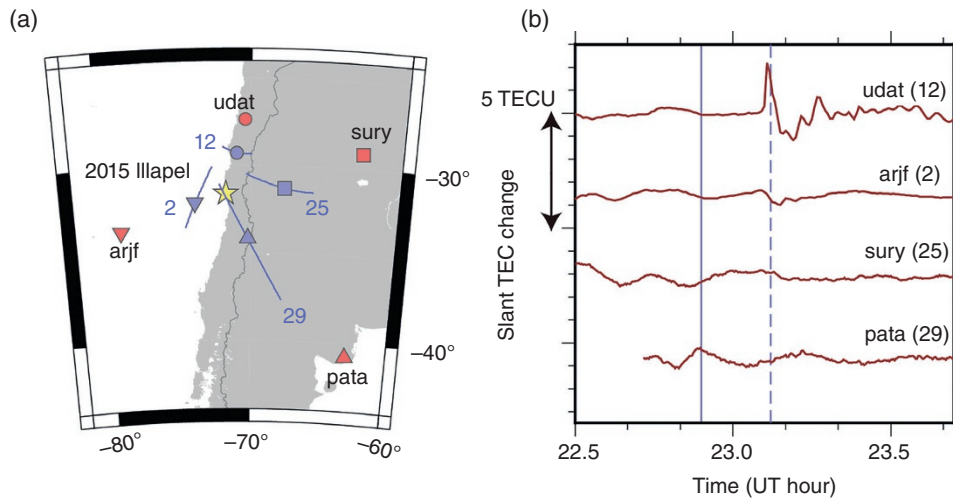
Figure 21.3 Comparison of the coseismic ionospheric disturbance of the 2015 Illapel earthquake, central Chile, propagating toward different directions (a). Their TEC time-series are given in (b) for those propagating toward the north, west, east, and south, from top to bottom. I selected satellite-site pairs with geometries of the epicenter (yellow), SIP (blue), GNSS station (red) favorable for coseismic ionospheric disturbance detections. Strong disturbance is seen only to the north of the epicenter. Numbers attached to the SIP tracks in (a) are satellite numbers (GPS).

Figure 21.3 compares TEC time series at stations located to the north, east, west, and south of the epicenter of the 2015 September Illapel earthquake (M_w8.3), central Chile. I used different satellites to realize shallow penetration angle of LOS to the acoustic wavefront. Figure 21.3b clearly shows that the strong coseismic ionospheric disturbance is seen only to the north of the epicenter, which is consistent with the expectation.

21.3.5. Magnitude Dependence

Rapid determination of M_w of earthquakes using the coseismic ionospheric disturbance amplitudes would enable us to infer tsunami size within ten minutes after the earthquake (Astafyeva et al., 2013). In the 2011 Tohoku-oki earthquake, the largest tsunami height at the coast occurred > 20 minutes later than the earthquake (see, e.g. Mitsui & Heki 2013). In such a case, TEC monitoring after large earthquakes may contribute to the early warning of tsunami.

In Figure 21.4, I show cases of 28 earthquakes with clear coseismic ionospheric disturbances of direct acoustic wave origin detected by GNSS observations. I selected the satellite-station pairs showing maximum disturbance amplitudes of individual earthquakes (i.e. pairs with small angles between LOS and wavefronts at the equator side of the epicenters). Their M_w range from 6.6 to 9.2, and the largest event is the 2004 Sumatra-Andaman earthquake. The smallest earthquake with successful ionospheric disturbance detection is the 2007 M_w6.6 Chuetsu-oki

earthquake, central Japan (Cahyadi & Heki, 2015), whose magnitude is close to the detection threshold suggested by Perevalova et al. (2014).

The 28 earthquakes include two normal fault earthquakes, i.e. the 2007 January central Kuril outer rise earthquake and the 2012 December Tohoku-oki outer rise earthquake. They also include two strike-slip earthquakes, i.e. the main shock and the largest aftershock of the 2012 North Sumatra earthquakes. The other 24 events are all reverse earthquakes. Twenty-one of the 28 examples in Figure 21.4 have been already reported in Cahyadi & Heki (2015), and the descriptions of newly added 7 earthquakes are available in He & Heki (2017).

The amplitudes of the ionospheric disturbances were derived from time series shown in Figure 21.4 with the same procedure as Cahyadi & Heki (2015). One may think it necessary to convert the STEC in Figure 21.4 to VTEC to compare the amplitudes of the disturbances. As shown in Figure 21.1, it is the incident angle of LOS with the wavefront rather than its zenith angle that governs the amplitudes of coseismic ionospheric disturbances and conversion to vertical TEC is unnecessary. Coseismic uplifts excite waves in neutral atmosphere, and it is necessary to normalize the amplitudes with the electron densities in the F region. Because altitude profiles of electron density are not always available, I used VTEC as the factor to normalize the amplitudes. Figure 21.5 compares "relative" ionospheric disturbance amplitudes in STEC normalized with the background VTEC.
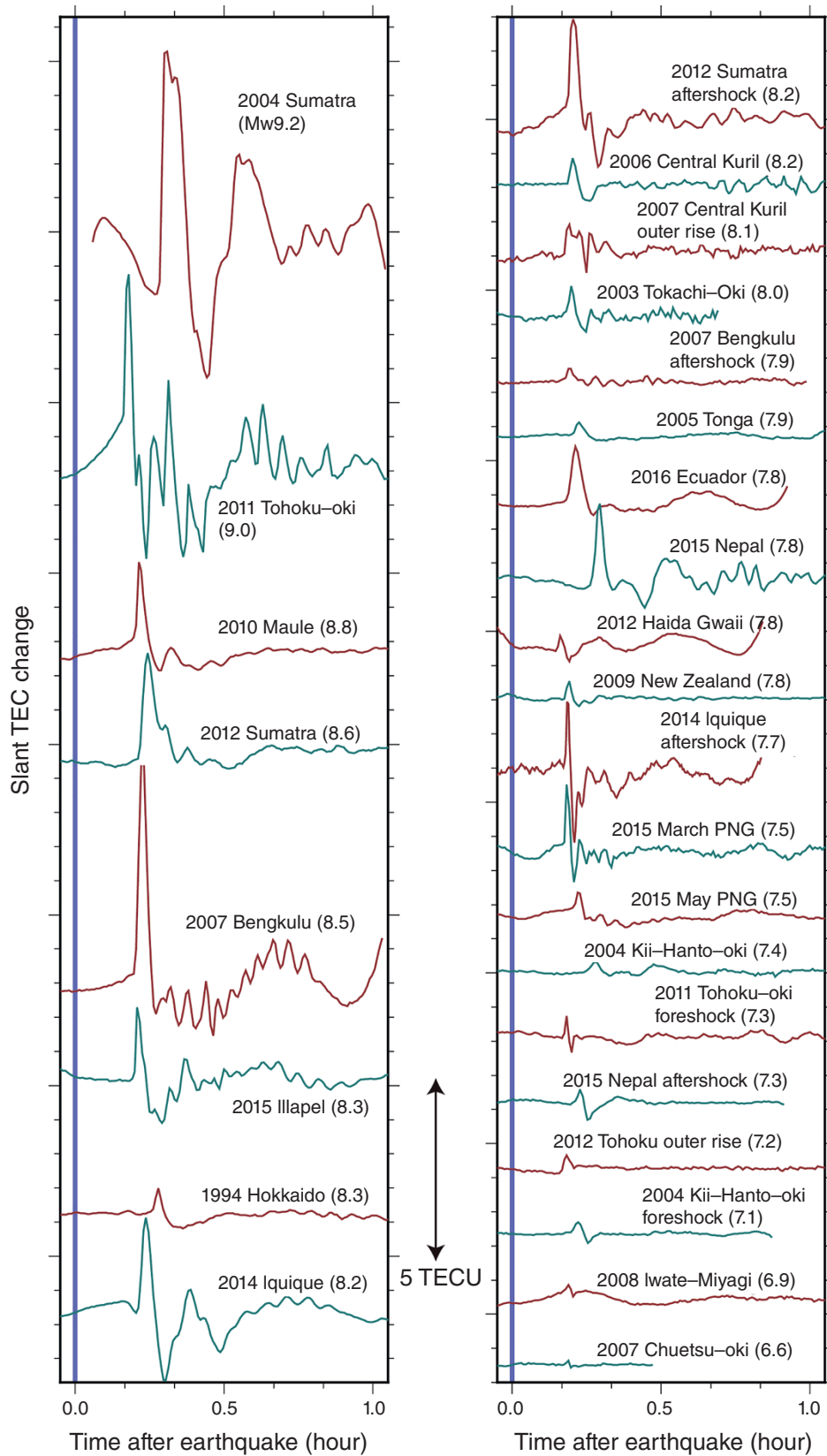
Figure 21.4 High-pass filtered STEC time-series of 28 examples of near-field coseismic ionospheric disturbance observations in the time window from −0.05 to 1.05 hours for earthquakes with M_w 9.2–8.2 (left) and 8.1–6.6 (right). Moment magnitudes are shown within the parentheses. For the satellite number and site names of 21 events reported earlier, see Table A1 of Cahyadi & Heki (2015). The station/satellite (GPS) of the eight new data are, 2015 Illapel (udat/12), 2014 Iquique (areq/01) and its aftershock (nzca/23), 2016 Ecuador (riop/06), 2015 Nepal (hyde/26) and its aftershock (lck4/19), 2015 March (pngm/10) and May (pngm/15) Papua New Guinea.
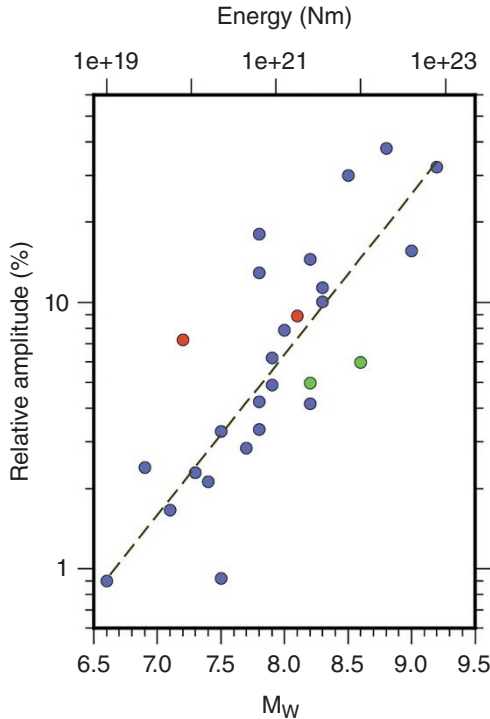
Figure 21.5 Comparison of M_w of the 28 earthquakes in Figure 21.4, with their ionospheric disturbance amplitudes in STEC relative to background VTEC. The dashed line indicates the best-fit line corresponding to Equation 21.2. Red and green shows normal and strike-slip earthquakes, respectively (others are reverse earthquakes).

I extend the discussion in Cahyadi & Heki (2015), and assume these amplitudes (unit: percent) obey a simple law,

$$\log_{10}(\text{Amplitude}) = a\,(M_w - 8.0) + b. \quad (21.2)$$

The offset b is the common logarithm of the relative amplitude of a typical $M_w 8$ event. The best-fit line inferred from all the earthquakes (dashed line in Figure 21.5) has the slope a of 0.602 with the 1σ uncertainty of 0.093, and b of 0.804 with the 1σ uncertainty of 0.057. Strike-slip earthquakes (green in Figure 21.5) show somewhat smaller amplitudes reflecting smaller vertical crustal movements for magnitudes (Cahyadi & Heki, 2015). Normal-fault earthquakes (red in Figure 21.5) do not show such a tendency. The slope a is close to 2/3, indicating that the disturbance amplitudes increase approximately by two orders of magnitude as M_w increases by three. This empirical law reflects the relationship between the maximum crustal uplift and M_w as shown in Figure A2 of Cahyadi & Heki (2015). Equation 21.2 enables us to infer M_w ~10 minutes after earthquakes by observing STEC oscillation relative to background VTEC in real time.

21.3.6. Far Field Disturbance

Direct acoustic waves decay rapidly with distance, and we can observe them only in the near-fields, say within 1,000 km of the epicenter. Secondary acoustic waves excited by Rayleigh surface waves (Figure 21.1) can reach farther distances owing to their smaller geometric decay. Ionospheric disturbances observed in California after the 2002 Denali earthquake, Alaska (Ducic et al., 2003), occurred by this mechanism. Examples of the 1994 Hokkaido-Toho-Oki earthquake (Figure 21.2a,d) also show smaller decay in distance for the faster components (Rayleigh wave origin) than the slower components (direct acoustic wave origin). Figure 21.6 gives another example of surface wave origin ionospheric disturbances observed in Japan ~40 minutes after the 2004 $M_w 9.2$ Sumatra-Andaman earthquake. Such data can be used to constrain group velocity of Rayleigh waves in the region without enough number of seismometers. Comprehensive studies of Rayleigh wave origin ionospheric disturbances are given in Rolland et al. (2011a).

21.4. PRESEISMIC IONOSPHERIC ANOMALIES

21.4.1. Discovery and Brief History of Debate

Heki (2011) found ionospheric TEC changes immediately before the 2011 March 11, $M_w 9.0$, Tohoku-oki earthquake using GEONET. The earthquake occurred in the afternoon (14:46 in local time), and VTEC showed gradual decrease. It started to present positive departure from the reference curve ~40 minutes before the earthquake (Figure 21.7a), and spatial distribution of such positive anomalies overlaps with the ruptured fault (Figure 21.7b,c).

It was also confirmed that similar TEC enhancements occurred before the 2004 Sumatra-Andaman ($M_w 9.2$), the 2010 Maule ($M_w 8.8$), and the 1994 Hokkaido-Toho-Oki ($M_w 8.3$) earthquakes (Heki, 2011), and the 2007 Bengkulu earthquake ($M_w 8.5$), Southern Sumatra (Cahyadi & Heki, 2013). Heki & Enomoto (2015) further added the main shock ($M_w 8.6$) and the largest aftershock ($M_w 8.2$) of the 2012 North Sumatra (Indian Ocean) earthquake, and the 2014 Iquique earthquake ($M_w 8.2$). They include most of the earthquakes with $M_w 8.2$ or more in this century except the 2005 Nias earthquake ($M_w 8.6$), where plasma bubble signatures hampered detections of any disturbances related to the earthquake. He & Heki (2017) analyzed VTEC behaviors before and after 32 earthquakes worldwide with $M_w 7.0$–8.0 in this century to reveal the lower limit of M_w of earthquakes showing preseismic TEC anomalies.
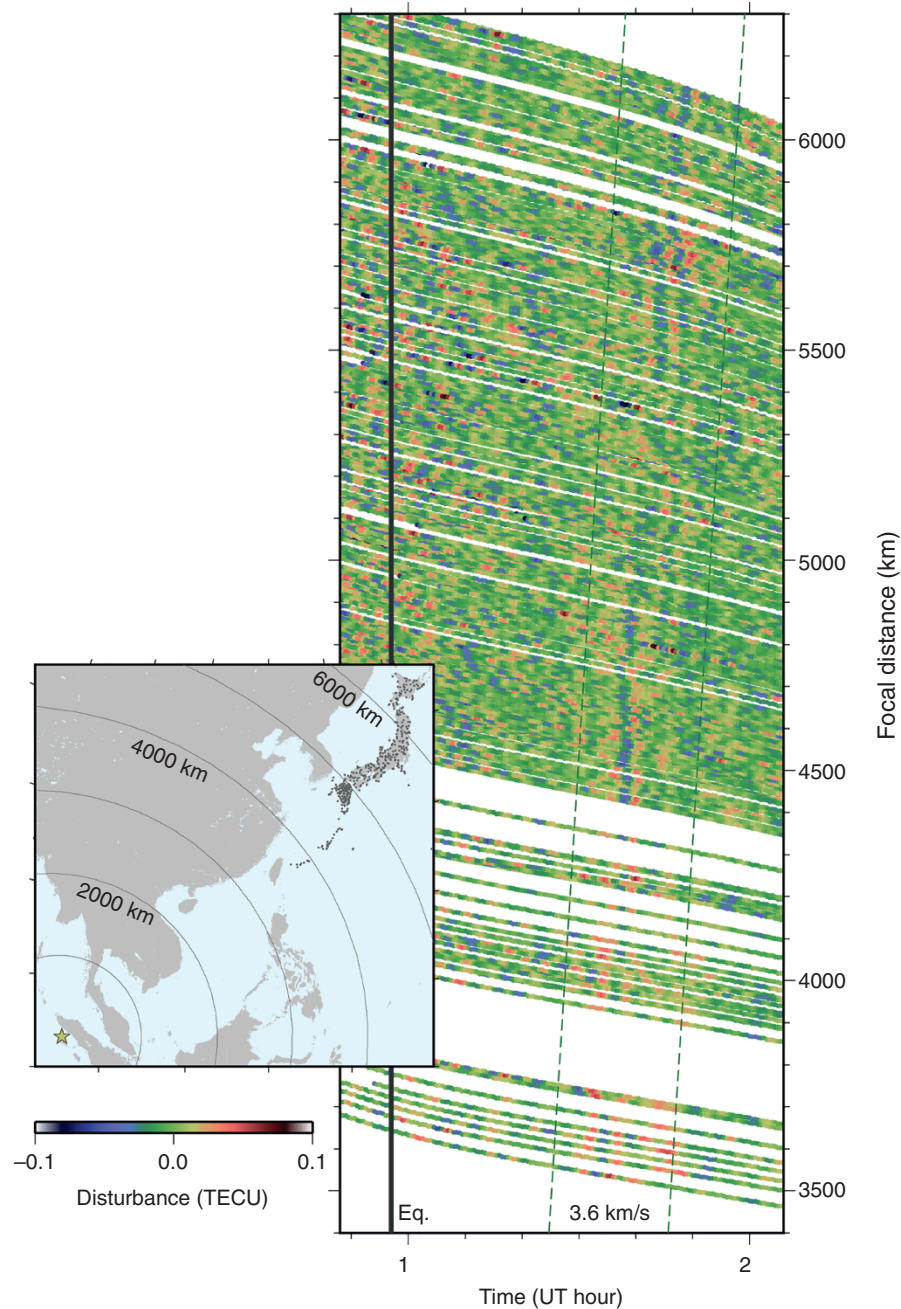
Figure 21.6 Distance-time diagram for the far-field ionospheric disturbances caused by Rayleigh surface wave of the 2004 Sumatra-Andaman earthquake (M_w9.2). They are observed using GPS satellite 13 with GEONET stations located 3,500–6,500 km from the epicenter. Weak but significant disturbances occur around the middle of the two dashed lines with slopes of 3.6 km/s.

Three papers critical to the preseismic ionospheric anomalies (Kamogawa and Kakinami, 2013; Utada and Shimizu, 2014; Masci et al., 2015) and rebuttals to them (Heki and Enomoto, 2013; 2014; 2015) have been published. Their criticisms concentrate on two points. First, they suspect that the preseismic TEC increase is an artifact popped up by defining the reference curves using the data not only before earthquakes but also after earthquakes.

An acoustic disturbance may result in long-lasting electron depletion above the tsunami source region (e.g. Kakinami et al., 2012), and Kamogawa & Kakinami (2013) consider that it influenced the definition of the reference curve. Secondly, they suspect that the anomalies originate from geomagnetic activities rather than earthquakes.

To rebut the first criticism, Heki & Enomoto (2015) demonstrated statistical significance of the preseismic
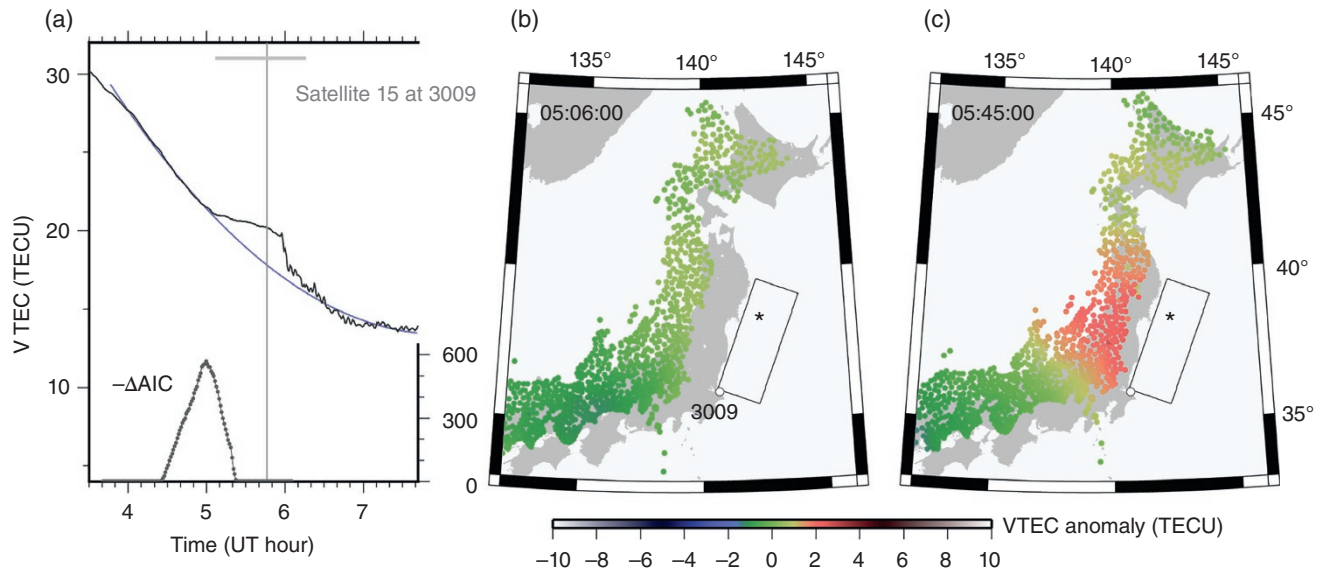
Figure 21.7 (a) Vertical TEC changes before and after the 2011 Tohoku-oki earthquakes (M_w9.0) observed with GPS satellite 15 at the 3009 station (see [b] for position). Reference curve (smooth gray curve) is obtained by fitting degree 2 polynomial of time to the VTEC time series excluding one-hour period encompasses the earthquake (gray horizontal line at the top). The significance of positive bending is expressed as -ΔAIC (Heki & Enomoto, 2015). Departure from the reference curve at two epochs, 40 minutes (b) and 1 minute (c) before the earthquake, are shown at their SIPs with colors. Positive anomalies (red color) appear near the ruptured fault (shown as the rectangle). Black star indicates the epicenter.

positive breaks (sudden increases of changing rates) in the VTEC trend using the Akaike's information criterion (AIC) using data only before earthquakes. Recently, Iwata & Umeno (2016) applied a new algorithm to detect preseismic TEC changes by calculating inter-station correlation of TEC anomalies, which serves as an additional rebuttal to the first criticism. To respond to the second criticism, Heki & Enomoto (2015) counted the occurrences of similar positive breaks in VTEC caused by space weather during times of no earthquakes and demonstrated it statistically unrealistic to attribute all the observed VTEC enhancements before large earthquakes to space weather.

21.4.2. 3D Distribution of the Anomalies

Heki (2011) and Heki & Enomoto (2013) pointed out that negative TEC changes started in areas further from the epicenters, simultaneously with positive TEC anomalies near the focal region, ~40 minutes before the 2011 Tohoku-oki earthquake. He & Heki (2016) studied the distributions of such pairs of negative and positive anomalies starting together before three large earthquakes in Chile, i.e. the 2010 Maule (M_w8.8), the 2014 Iquique (M_w8.2), and the 2015 Illapel (M_w8.3) earthquakes (Figure 21.8) and suggested that they occur in higher and lower parts of ionosphere.

He & Heki (2018) did 3D tomography of the ionosphere using STEC anomalies of the 2015 Illapel earthquake and

confirmed that (1) positive and negative electron density anomalies appeared at lower (Figure 21.9a) and higher (Figure 21.9b) altitudes of the ionosphere, respectively; and (2) they roughly line up along the local geomagnetic field (Figure 21.9c). This 3D structure suggests that the anomalies are generated by downward plasma transportation caused by $\mathbf{E} \times \mathbf{B}$ drifts of electrons. Because the electron density has its maximum at ~300 km, uniform downward electron transportation would make a pair of positive/negative anomalies below/above this height (Kuo et al., 2014). A similar study was done for the 2011 Tohoku-oki earthquake (Muafiry & Heki, 2020).

Kelley et al. (2017) discussed quantitative requirements to enable the ~10 % TEC anomalies before the 2011 Tohoku-oki earthquake by $\mathbf{E} \times \mathbf{B}$ drifts. They thought this could be achieved by downward displacement of electrons by ~20 km. If this occurred in 40 minutes, the electron velocity would be 8 m/s, and the required electric field is 0.5 mV/m. They further inferred that surface electric fields to make this field would not exceed 0.2 V/m. This is much smaller than the fair weather electric field and difficult to detect with pre-existing sensors, which is consistent with the lack of reports of strong vertical electric fields at the surface before large earthquakes. Actual electron drift occurs perpendicular to $\mathbf{B}$, but the required displacements (20 km before the 2011 Tohoku-oki) are smaller than the voxel size of the 3D tomography in Figure 21.9.

If this scenario is correct, similar electron density anomalies are expected to occur above the geomagnetic
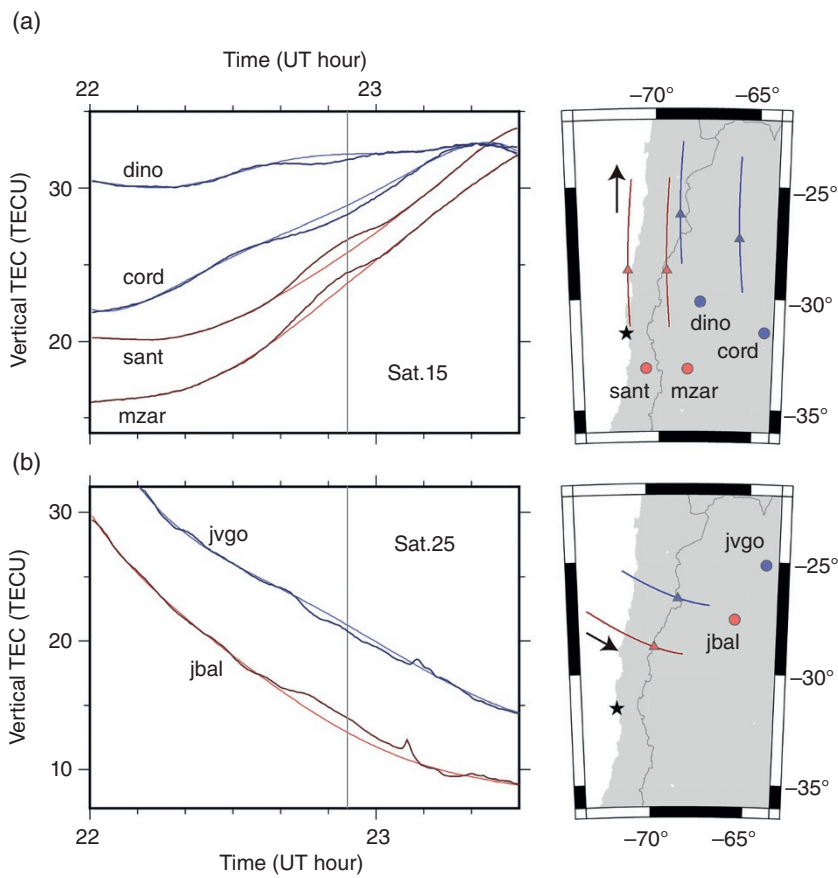
Figure 21.8 VTEC changes before and after the 2015 Illapel earthquake (M$_w$8.3), central Chile, observed with GPS satellites 15 (a) and 25 (b) showing simultaneous start of positive (red curves) and negative (blue curves) changes starting ~15 minutes before the earthquake (vertical lines) (He & Heki, 2016). Departures from reference curves at various epochs are used as inputs to 3D tomography of electron density anomalies (Figure 21.9).
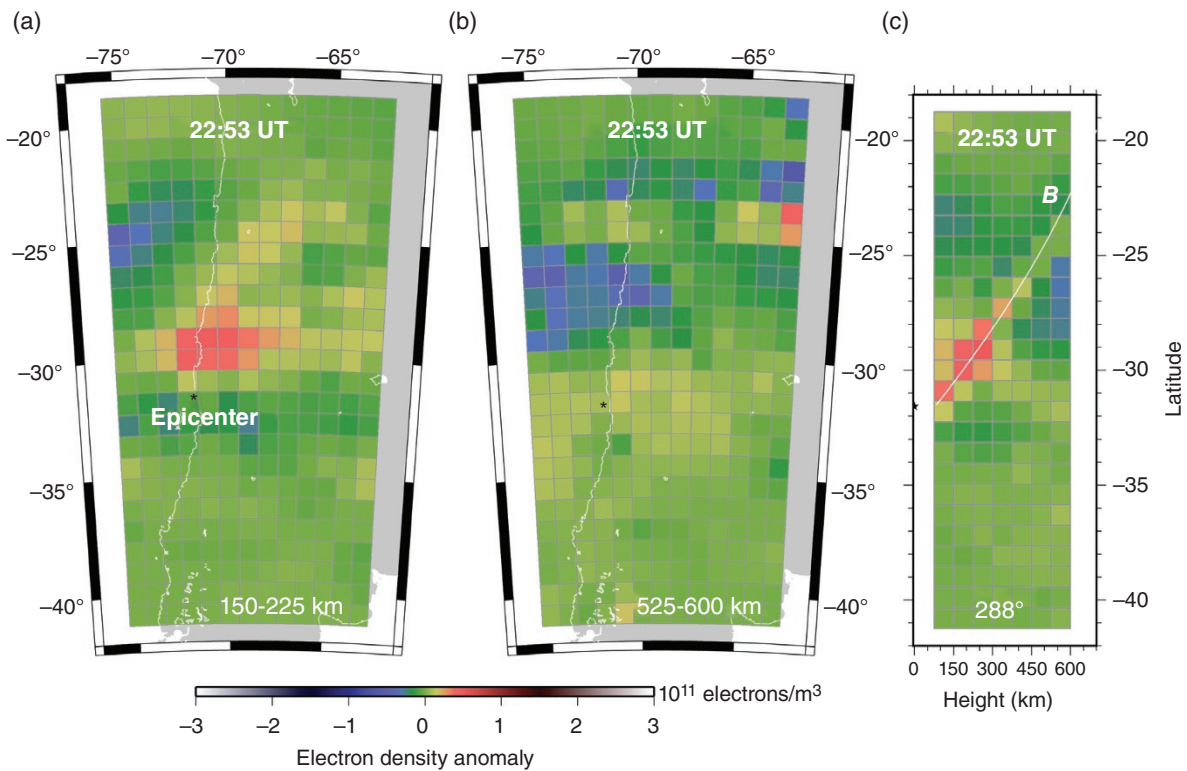

Figure 21.9 Results of 3D tomography of electron density anomalies at heights from 75 km to 600 km, one minute before the 2015 Illapel earthquake (22:53 UT, September 16). (a) and (b) indicate horizontal map at altitude ranges 150–225 km and 525–600 km, respectively. The white curves show coastlines and the black star indicates the epicenter. (c) is the north-south profile at longitude 288E. Local geomagnetic field line is given with a white curve in (c). For detail including the checker-board resolution test, see He & Heki (2018).

conjugate point of the epicenter (Kuo et al., 2014). He & Heki (2018) looked for such conjugate anomalies for the 2015 Illapel earthquake but did not reach a decisive conclusion.

Origin of the hypothetical surface electric charges is yet to be explored, but peroxy defects and positive holes in rocks would be a possibility. Laboratory experiments showed that positive holes are mobilized by micro-cracks and micro-dislocations in highly stressed rocks (e.g. Freund, 2013). Such mobilized positive charges would concentrate on the surface, with its areal density determined by the balance between the charge generation rate and its decay rate (diffusion to surroundings). The land–ocean electric conductivity contrast suggests that the charge may concentrate on land. Such positive hole mobilization may not be the only candidate to make electric fields penetrate the ionosphere. Future studies are needed to clarify the polarization process of crustal electric charges bridging gap between laboratory and real faults.

21.4.3. Magnitude Dependence and Shapes of Preseismic Signatures

Any phenomena related to earthquakes should depend on their magnitudes. Therefore, clear M_w dependence of preseismic anomalies would provide a firm support for their reality as an earthquake precursor. So far, three kinds of M_w dependence have been reported for the ionospheric changes immediately before large earthquakes. Heki & Enomoto (2015) found that the amount of the preseismic VTEC rate changes depend on M_w, and that earthquakes with larger M_w tend to have longer precursor times (i.e. they start earlier). Then, He & Heki (2016) showed that the anomalies of larger earthquakes have larger spatial dimensions. In Figure 21.10, I compare preseismic VTEC anomalies from 18 examples with M_w ranging from 7.3 to 9.2 compiled from Heki & Enomoto (2015) and He & Heki (2017). The figure shows that typical leading times of M_w9 and 8 earthquakes are ~45 minutes and ~15 minutes, respectively. We need to normalize the curves in this figure by their background VTEC values to compare cumulative VTEC anomalies between different earthquakes. They are typically a few percent for M_w8 class earthquakes while they may exceed 10 percent for M_w9 class events. This explains why we can detect such anomalies before M_w8 class events only when VTEC values are high.

Figure 21.11 shows the "standard" VTEC change curve of the 18 examples after normalizing them by cumulative amount of the anomalies (vertical axis) and by precursor times (only parts before earthquakes) (horizontal axis). In doing so, I use the cumulative amplitudes and leading times of individual earthquakes, as shown in Figure 21.10. Then I calculate the median (blue) and
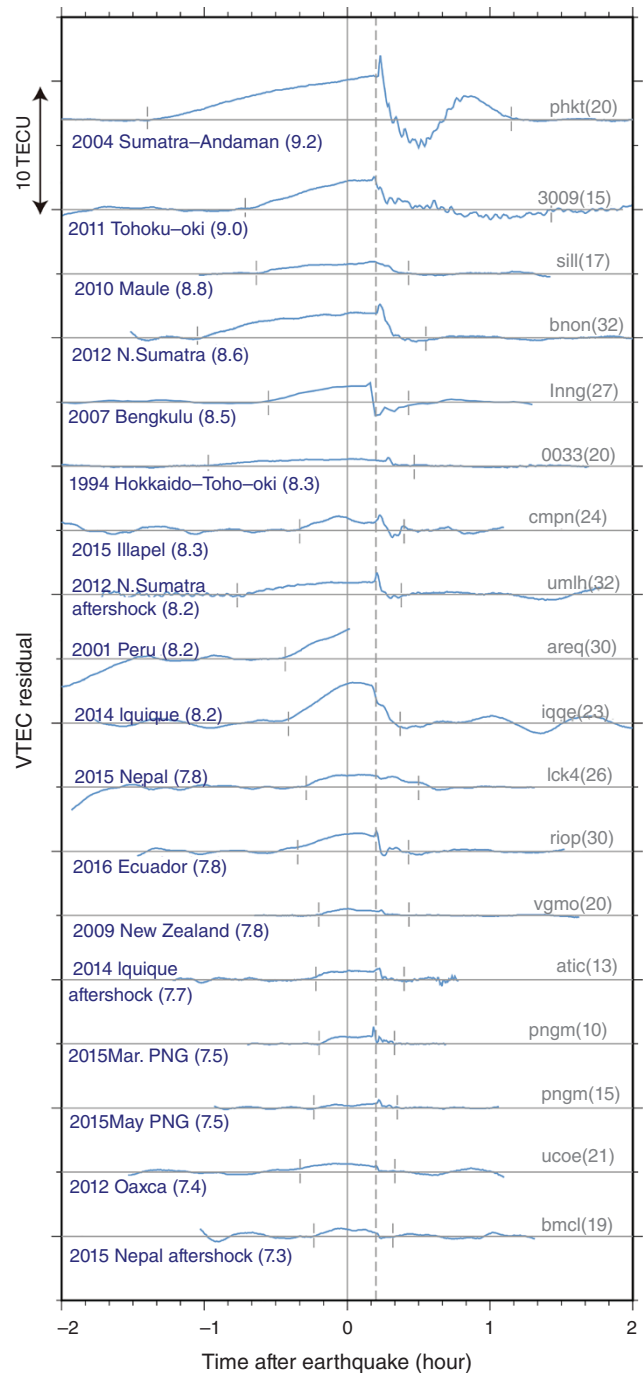

Figure 21.10 VTEC anomalies (departure from reference curves) before and after 18 earthquakes with M_w from 7.3 to 9.2 observed with GNSS (Heki & Enomoto, 2015; He & Heki, 2017). They are characterized by gradual preseismic increase and postseismic decay overprinted with acoustic disturbances starting ~10 minutes after earthquakes (vertical dashed line). Larger earthquakes show longer leading times as well as larger positive anomalies. Station names and GNSS (only GPS are used) satellite numbers are shown to the right of the curves. Short vertical bars denote the onsets of the preseismic anomalies.
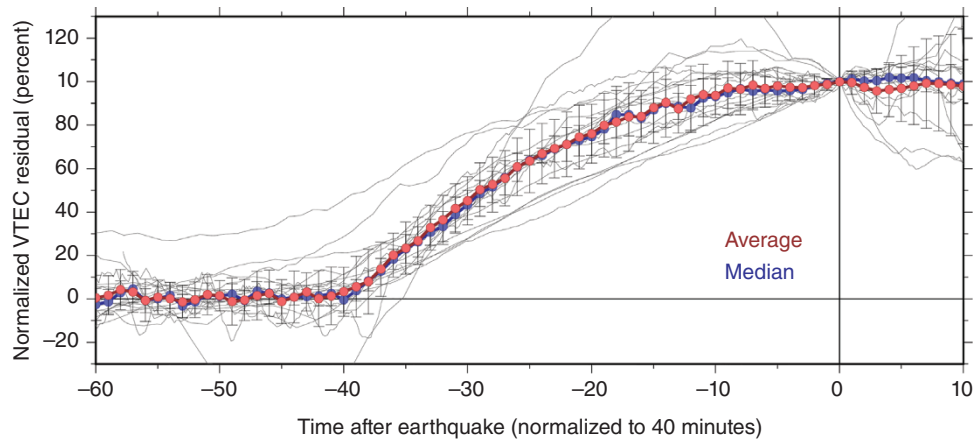
Figure 21.11 VTEC change curves of 18 earthquakes shown in Figure 21.10 (thin gray curves) and their stacked (blue: median, red: average) curves. Before stacking, their cumulative anomalies in the vertical axis are normalized to 100 %. The horizontal axis (time) is also normalized so that the leading times of all the cases coincide with 40 minutes (the time axis normalization is done only for negative domain of time). Error bars show 1σ standard deviation (average) and quartile (median). The standard curve shows distinct start with slowly decaying rate. After earthquakes, VTEC does not increase further, and remains stationary until acoustic disturbance arrivals.

the average (red) of all the cases to define the standard curve.

The first feature of this curve appears in the negative time (preseismic part), i.e. they show distinct start and gradual decay of the rate. This contradicts to general images of earthquake precursors that they start gently and accelerate toward earthquakes, e.g. preseismic crustal uplift suggested to have occurred before the main rupture of the 1944 Tonankai earthquake in central Japan (Mogi, 1984). The second feature is that VTEC does not show further increase after occurrences of the earthquakes. It does not show rapid decay either. It just remains stationary until the acoustic disturbance arrives at ~10 minutes after earthquakes.

The first point (upward convex VTEC increase curve) would indicate that the build-up of surface positive electric charges occurs together with decay proportional to the cumulative charges. Such a decay would occur by their leakage of surface charges especially to ocean. This is just like pouring water at a constant rate into a bucket with a hole at its bottom. The drain from the hole will increase as the water level increases, and the water level reaches the maximum when the input and output are balanced. The water level in the bucket would increase as $\exp(1-e^{-t/\tau})$, just like in Figure 21.11, where t is time after the start of impoundment, and τ is the time constant.

The second point (stationary after earthquakes) means that VTEC anomaly still exists for ten minutes or more after earthquake released the crustal stress and stopped further electric charge mobilization. This may look puzzling because the surface electric charge would rapidly decay by diffusing into ocean (water level would drop fast

if we stop the supply of water into a broken bucket). After the crust-origin ionospheric electric field disappears in the ionosphere, decays of positive and negative electron density anomalies, as seen in Figure 21.9, would be left for natural gradual decay. The VTEC anomalies may therefore stay for a certain length of time rather than disappearing immediately.

21.5. CONCLUDING REMARKS

In this chapter, I reviewed ionospheric disturbances related to earthquakes, observation and data analysis technique, near- and far-field coseismic disturbances, and possible short-term preseismic anomalies. The study of coseismic disturbances would contribute to early tsunami warning by their real-time observations and rapid determination of M_w before tsunami arrivals. The study of preseismic ionospheric anomalies would contribute to the investigation of seismogenesis and eventually to short-term earthquake prediction.

Rapid progress in this field owes much to the recent densification of GNSS receivers in regions close to boundaries of tectonic plates. Such dense networks helped us investigate spatial distribution and temporal evolution of ionospheric anomalies related to earthquakes in depth. Conventional ionospheric sensors such as ionosonde cannot provide such detailed information because of their sparse distribution. In fact, only 4 ionosonde stations are available in Japan while ~1200 GNSS stations are operational, and each of them track tens of GNSS satellites almost continuously.

Increasing the number of GNSS other than GPS would further accelerate the advance of the study of co- and pre-seismic ionospheric disturbances. In the future, new types of sensors, e.g. over-the-horizon (OTH) radar (Occhipinti et al., 2010; Roy et al., 2014) and interferometric synthetic aperture radar (InSAR) (Furuya et al., 2017), have potential to provide unique information on ionospheric disturbances related to earthquakes with spatial resolution higher than current GNSS networks.

ACKNOWLEDGMENTS

REFERENCES

Astafyeva, E., Heki, K., Kiryushkin, V., Afraimovich, E., & Shalimov, S. (2009). Two-mode long-distance propagation of coseismic ionosphere disturbances. *Journal of Geophysical Research*, 114, A10307. doi:10.1029/2008JA013853

Astafyeva, E., Rolland, L., Lognonné, P., Khelfi, K., & Yahagi, T. (2013). Parameters of seismic source as deduced from 1 Hz ionospheric GPS data: Case study of the 2011 Tohoku-oki event. *Journal of Geophysical Research*, 118, 5942–5950. doi:10.1002/jgra.50556

Blanc, E. (1983). Observations in the upper atmosphere of infrasonic waves from natural or artificial sources – A summary. *Annales Geophysicae*, 3, 673–687.

Cahyadi, M. N., & Heki, K. (2013). Ionospheric disturbances of the 2007 Bengkulu and the 2005 Nias earthquakes, Sumatra, observed with a regional GPS network. *Journal of Geophysical Research*, 118, 1–11. doi:10.1002/jgra.50208

Cahyadi, M. N., & Heki, K. (2015). Coseismic ionospheric disturbance of the large strike-slip earthquakes in North Sumatra in 2012: M_w dependence of the disturbance amplitudes. *Geophysical Journal International*, 200, 116–129.

Calais, E., & Minster, J. B. (1995). GPS detection of ionospheric perturbations following the January 17, 1994, Northridge earthquake. *Geophysical Research Letters*, 22, 1045–1048. doi:10.1029/95GL00168

Choosakul, N., Saito, A., Iyemori, T., & Hashizume, M. (2009). Excitation of 4-min periodic ionospheric variations following the great Sumatra-Andaman earthquake in 2004. *Journal of Geophysical Research*, 114, A10313. doi:10.1029/2008JA013915

Ducic, V., Artru, J., & Longnonné, P. (2003). Ionospheric remote sensing of the Denali Earthquake Rayleigh surface wave. *Geophysical Research Letters*, 30, 1951. doi:10.1029/2003GL017812

Freund, F. (2013). Earthquake forewarning - A multidisciplinary challenge from the ground up to space. *Acta Geophysica*, 6(14), 775–807. doi:10.2478/s11600-013-0130-4

Furuya, M., Suzuki, T., Maeda, J., & Heki, K. (2017). Midlatitude sporadic-E episodes viewed by L-band split-spectrum InSAR. *Earth Planets Space*, 69, 175. doi:/10.1186/s40623-017-0764-6

Hayakawa, M., Molchanov, O. A., Ondoh, T., & Kawai, E. (1996). On the precursory signature of Kobe earthquake in subionospheric VLF propagation. *Journal of the Communications Research Laboratory*, 43, 169–180.

He, L., & Heki, K. (2016). Three-dimensional distribution of ionospheric anomalies prior to three large earthquakes in Chile. *Geophysical Research Letters*, 43(14), 7287–7293. doi:10.1002/2016GL069863

He, L. & Heki, K. (2017). Ionospheric anomalies immediately before M_w 7.0-8.0 earthquakes. *Journal of Geophysical Research: Space Physics*, 122, 8659–8678. doi:10.1002/2017JA024012

He, L. & Heki, K. (2018). Three-dimensional tomography of ionospheric anomalies immediately before the 2015 Illapel earthquake, central Chile. *Journal of Geophysical Research: Space Physics*, 123. doi:10.1029/2017JA024871

Heki, K. (2006). Explosion energy of the 2004 eruption of the Asama Volcano, Central Japan, inferred from ionospheric disturbances. *Geophysical Research Letters*, 33, L14303. doi:10.1029/2006GL026249

Heki, K., (2011). Ionospheric electron enhancement preceding the 2011 Tohoku-Oki earthquake. *Geophysical Research Letters*, 38, L17312. doi:10.1029/2011GL047908

Heki, K., & Ping, J.-S. (2005). Directivity and apparent velocity of the coseismic ionospheric disturbances observed with a dense GPS array. *Earth and Planetary Science Letters*, 236, 845–855.

Heki, K., Otsuka, Y., Choosakul, N., Hemmakorn, N., Komolmis, T., & Maruyama, T. (2006). Detection of ruptures of Andaman fault segments in the 2004 great Sumatra earthquake with coseismic ionospheric disturbances. *Journal of Geophysical Research*, 111, B09313. doi:10.1029/2005JB004202

Heki, K. & Enomoto, Y. (2013). Preseismic ionospheric electron enhancements revisited. *Journal of Geophysical Research*, 118, 6618–6626. doi:10.1002/jgra.50578

Heki, K., & Enomoto, Y. (2014). Reply to comment by K. Heki & Y. Enomoto on "Preseismic ionospheric electron enhancements revisited." *Journal of Geophysical Research: Space Physics*, 119. doi:10.1002/2014JA020223

Heki, K., & Enomoto, Y. (2015). M_w dependence of preseismic ionospheric electron enhancements. *Journal of Geophysical Research: Space Physics*, 120, 7006–7020. doi:10.1002/2014JA020223

Iwata, T., & Umeno, K. (2016). Correlation Analysis for Preseismic Total Electron Content Anomalies around the 2011 Tohoku-Oki Earthquake. *Journal of Geophysical Research: Space Physics*, 121, 8969–8984. doi:10.1002/2016JA023036

Iyemori, T., Nose, M., Han, D., Gao, Y., Hashizume, M., Choosakul, N., et al. (2005). Geomagnetic pulsation caused by the Sumatra earthquake on December 26, 2004. *Geophysical Research Letters*, 32, L20807. doi:10.1029/2005GL024083

Kakinami, Y., Kamogawa, M., Tanioka, Y., Watanabe, S., Gusman, A. R., Liu, J.-Y., et al. (2012). Tsunamigenic ionospheric hole. *Geophysical Research Letters*, 39, L00G27. doi:10.1029/2011GL050159

Kamogawa, M., & Kakinami, Y. (2013). Is an ionospheric electron enhancement preceding the 2011 Tohoku-oki earthquake a precursor? *Journal of Geophysical Research*, 118, 1–4. doi:10.1002/jgra.50118

Kelley, M. C., Swartz, W. E., & Heki, K. (2017). Apparent ionospheric total electron content variations prior to major

earthquakes due to electric fields created by tectonic stresses. *Journal of Geophysical Research: Space Physics*, *122*. doi:10.1002/2016JA023601

Kuo, C. L., Lee, L. C., & Huba, J. D. (2014). An improved coupling model for the lithosphere-atmosphere-ionosphere system. *Journal of Geophysical Research: Space Physics*, *119*, 3189–3205. doi:10.1002/2013JA019392

Le, H., Liu, J. Y., & Liu, L. (2011). A statistical analysis of ionospheric anomalies before 736 M6.0+ earthquakes during 2002–2010. *Journal of Geophysical Research*, *116*, A02303. doi:10.1029/2010JA015781

Le Pichon, A., Henry, P., Mialle, P., Vergoz, J., Brachet, N., Garcés, M., et al. (2005). Infrasound associated with 2004–2005 large Sumatra earthquakes and tsunami. *Geophysical Research Letters*, *32*, L19802. doi:10.1029/2005GL023893

Li, M., & Parrot, M. (2013). Statistical analysis of an ionospheric parameter as a base for earthquake prediction. *Journal of Geophysical Research*, *118*, 3731–3739. doi:10.1002/jgra.50313

Liu, J. Y., Chen, Y. I., Chuo, Y. J., & Tsai, H. F. (2011). Variations of ionospheric total electron content during the Chi-Chi earthquake. *Geophysical Research Letters*, *28*, 1383–1386.

Maeda, J., & Heki, K. (2015). Morphology and dynamics of daytime mid-latitude sporadic-E plasma patches revealed by GPS total electron content observations in Japan. *Earth Planets Space*, *67*, 89. doi:10.1186/s40623-015-0257-4

Mannucci, A. J., Wilson, B. D., Yuan, D. N., Ho, C. H., Lindqwister, U. J., & Runge, T. F. (1998). A global mapping technique for GPS-derived ionospheric total electron content measurements. *Radio Science*, *33*, 565–582. doi:10.1029/97RS02707

Masci, F., Thomas, J., Villani, F., Secan, J., & Rivera, N. (2015). On the onset of ionospheric precursors 40 min before strong earthquakes. *Journal of Geophysical Research: Space Physics*, *120*(2), 1383–1393. doi:10.1002/2014JA020822

Mitsui, Y., & Heki, K. (2013). Scaling of early afterslip velocity and possible detection of tsunami-induced subsidence by GPS measurements immediately after the 2011 Tohoku-Oki earthquake. *Geophysical Journal International*, *195*, 238–248. doi:10.1093/gji/ggt256

Mogi, K. (1984). Temporal variation of crustal deformation during the days preceding a thrust-type great earthquake – The 1944 Tonankai earthquake of magnitude 8.ll, Japan. *Pure and Applied Geophysics*, *122*, 765–780.

Muafiry, I. N., & Heki, K. (2020). 3D tomography of the ionospheric anomalies immediately before and after the 2011 Tohoku-oki (M_w9.0) earthquake. *Journal of Geophysical Research: Space Physics*, *125*. doi:10.1029/2020JA027993

Nakashima, Y., Heki, K., Takeo, A., Cahyadi, M. N., Aditiya, A., & Yoshizawa, K. (2016). Atmospheric resonant oscillations by the 2014 eruption of the Kelud volcano, Indonesia, observed with the ionospheric Total Electron Contents and seismic signal. *Earth and Planetary Science Letters*, *434*, 112–116.

Němec, F., Santolik, O., Parrot, M., & Berthelier, J. J. (2008). Spacecraft observations of electromagnetic perturbations connected with seismic activity. *Geophysical Research Letters*, *35*, L05109. doi:10.1029/2007GL032517

Nishida, K., Kobayashi, N., & Fukao, Y. (2000). Resonant oscillation between the solid earth and the atmosphere. *Science*, *287*, 2244–2246.

Occhipinti, G., Lognonné, P., Kherani, E. A., & Hébert, H. (2006). Three-dimensional waveform modelling of ionospheric signature induced by the 2004 Sumatra tsunamis. *Geophysical Research Letters*, *33*, L20104. doi: 10.1029/2006GL026865

Occhipinti, G., Dorey, P., Farges, T., & Lognonné, P. (2010). Nostradamus: The radar that wanted to be a seismometer. *Geophysical Research Letters*, *37*, L18104. doi:10.1029/2010GL044009

Otsuka, Y., Kotake, N., Tsugawa, T., Shiokawa, K., Ogawa, T., Effendy, S., et al. (2006). GPS detection of total electron content variations over Indonesia and Thailand following the 26 December 2004 earthquake. *Earth Planets Space*, *58*(2), 159–165.

Otsuka, Y., Kotake, N., Shiokawa, K., Ogawa, T., Tsugawa, T., & Saito, A. (2011). Statistical study of medium-scale traveling ionospheric disturbances observed with a GPS receiver network in Japan. In *Aeronomy of the Earth's Atmosphere and Ionosphere*, edited by M. A. Abdu and D. Pancheva, *IAGA Special Sopron Book Series 2*. Springer. doi:10.1007/978-94-007-0326-1_21

Perevalova, N. P., Sankov, V. A., Astafyeva, E. I., & Zhupityaeva, A. S. (2014). Threshold magnitude for ionospheric TEC response to earthquakes. *Journal of Atmospheric and Solar-Terrestrial Physics*, *108*, 77–90.

Rideout, W., & Coster, A. (2006). Automated GPS processing for global total electron content data. *GPS Solutions*, *10*, 219–228. doi:10.1007/s10291-006-0029-5

Rolland, L. M., Lognonné, P., & Munekane, H. (2011a). Detection and modeling of Rayleigh wave induced patterns in the ionosphere. *Journal of Geophysical Research*, *116*, A05320. doi:10.1029/2010JA016060

Rolland, L. M., Lognonné, P., Astafyeva, E., Kherani, E. A., Kobayashi, N., Mann, M., & Munekane, H. (2011b). The resonant response of the ionosphere imaged after the 2011 off the Pacific coast of Tohoku earthquake. *Earth Planets Space*, *63*, 853–857.

Rolland, L. M., Vergnolle, M., Nocquet, J.-M., Sladen, A., Dessa, J.-X., Tavakoli, F., et al. (2013). Discriminating the tectonic and non-tectonic contributions in the ionospheric signature of the 2011, M_w7.1, dip-slip Van earthquake, Eastern Turkey. *Geophysical Research Letters*, *40*, 2518–2522. doi:10.1002/grl.50544

Roy, C., Occhipinti, G., Boschi, L., Molinié, J.-P., & Wieczorek, M. (2014). Effect of ray and speed perturbations on ionospheric tomography by over-the-horizon radar: A new method. *Journal of Geophysical Research*, *119*, 7841–7857. doi:10.1002/2014JA020137

Saito, A., Fukao, S., & Miyazaki, S. (1998). High resolution mapping of TEC perturbations with the GSI GPS network over Japan. *Geophysical Research Letters*, *25*, 3079–3082.

Saito, A., Tsugawa, T., Otsuka, Y., Nishioka, M., Iyemori, T., Matsumura, M., et al. (2011). Acoustic resonance and plasma depletion detected by GPS total electron content observation after the 2011 off the Pacific coast of Tohoku Earthquake. *Earth Planets Space*, *63*, 863–867.

Shinagawa, H., Iyemori, T., Saito, S., & Maruyama, T. (2007). A numerical simulation of ionospheric and atmospheric variations associated with the Sumatra earthquake on December 26, 2004. *Earth Planets Space*, *59*, 1015–1026.

Shinagawa, H., Tsugawa, T., Matsumura, M., Iyemori, T., Saito, A., Maruyama, T., et al. (2013). Two-dimensional simulation of ionospheric variations in the vicinity of the epicenter of the Tohoku-Oki earthquake on 11 March 2011. *Geophysical Research Letters*, *40*, 5009–5013. doi:10.1002/2013GL057627

Shults, K., Astafyeva, E., & Adourian, S. (2016). Ionospheric detection and localization of volcano eruptions on the example of the April 2015 Calbuco events. *Journal of Geophysical Research*, *121*, 10,303–10,315. doi:10.1002/2016/JA023382

Tahira, M. (1995). Acoustic resonance of the atmospheric at 3.7 mHz. *Journal of the Atmospheric Sciences*, *52*, 2670–2674.

Tanaka, T., Ichinose, T., Okusawa, T., Shibata, T., Sato, Y., Nagasawa, C., & Ogawa, T. (1984). HF Doppler observations of acoustic wave exhibited by the Urakawa-Oki earthquake on 21 March 1982. *Journal of Atmospheric and Terrestrial Physics*, *46*, 233–245.

Tanimoto, T., Heki, K., & Artru-Lambin, J. (2015). Interaction of Solid Earth, Atmosphere, and Ionosphere. In *Treatise on Geophysics, 2nd edition, Vol 4*, edited by G. Schubert, Oxford: Elsevier, pp. 421–443.

Thomas, J.N., Huard, J., & Masci, F. (2017). A statistical study of global ionospheric map total electron content changes prior to occurrences of $M{\geq}6.0$ earthquakes during 2000–2014. *Journal of Geophysical Research*, *122*, 2151–2161. doi:10.1002/2016JA023652

Tsugawa, T, Saito, A., Otsuka, Y., Nishioka, M., Maruyama, T., Kato, H., et al. (2011). Ionospheric disturbances detected by GPS total electron content observation after the 2011 off the Pacific coast of Tohoku Earthquake. *Earth Planets Space*, *63*, 875–879.

Utada, H., & Shimizu, H. (2014). Comment on "Preseismic ionospheric electron enhancements revisited" by K. Heki and Y. Enomoto, *Journal of Geophysical Research: Space Physics*, *119*(7), 6011–6015. doi:10.1002/2014JA020044

Yuen, P. C., Weaver, P. F., & Suzuki, R. K. (1969). Continuous, traveling coupling between seismic waves and the ionosphere evident in May 1968 Japan earthquake data. *Journal of Geophysical Research*, *74*, 2256–2264.